Geophys. J. Int. (2002) **149,** 440–453

Determination of the influence zone for surface wave paths

K. Yoshizawa and B. L. N. Kennett

Research School of Earth Sciences, The Australian National University, Canberra ACT 0200, *Australia. E-mail: kazu@rses.anu.edu.au*

Accepted 2001 November 22. Received 2001 November 8; in original form 2001 February 7

SUMMARY

An approximate description of the zone of influence around the propagation path for a surface wave is provided by investigating the Fresnel zones for the frequency range of interest. The influence zone about surface wave paths, over which surface waves are coherent in phase, is identified as approximately one-third of the width of the first Fresnel zone. A technique called Fresnel-area ray tracing (FRT) for surface waves has been used to estimate this region around the ray path for each frequency. The FRT technique is developed by combining two standard ray tracing methods, i.e. kinematic ray tracing (KRT) and dynamic ray tracing (DRT). To obtain the exact Fresnel area in a laterally heterogeneous structure would require the solution of a large number of KRT equations. In contrast, the FRT approach requires just a few ray tracing calculations. In the first step, the trajectory of the surface wave is computed by solving the KRT system for the phase-velocity distribution at the required frequency. In the next step, the behaviour of rays in the zone surrounding the KRT path is calculated by solving the DRT system twice; once from the source to the receiver and once more from the receiver to the source along the same trajectory. Finally, combining the solutions of these ray tracing systems using paraxial ray theory, the Fresnel area around a central ray can be estimated. Using FRT, stationary-phase fields can be constructed around a central ray path in a laterally heterogeneous structure. The influence zone around the ray path is then estimated from the stationary-phase function with simple assumptions concerning the perturbed wavefield. The estimate of the influence zone can be efficiently calculated in laterally heterogeneous structure by using the FRT technique, and allows an extension of current methods of surface wave analysis, which have commonly been based on geometrical ray theory and on the approximation of great-circle propagation. This approach allows the treatment of finite-width rays as well as deviations in propagation from the great circle induced by moderate lateral heterogeneity as revealed by recent tomography models. Such finite-width rays should be of major benefit in enhancing ray-based surface wave tomography.

Key words: Fresnel zone, ray theory, ray tracing, surface wave, tomography.

1 INTRODUCTION

Geometrical ray theory has played a major role in many seismological studies because of its simple and efficient description of seismic wave propagation. One of the most successful applications of ray theory is seismic tomography and a number of Earth models have been obtained by applying the theory to both body and surface waves. Such studies for investigating the Earth's interior based on ray theory have provided us with an enormous amount of knowledge concerning the structure and dynamics of the mantle. There are, however, crucial limitations in the ray theory.

One of the well-known deficiencies of ray theory is that the theory tends to breakdown in the presence of strong lateral heterogeneity when the scalelength is comparable to the wavelength of the waves. Wang & Dahlen (1995) have obtained an empirical condition for the validity of surface wave ray theory by comparing phase, arrival angle and amplitude anomalies obtained from WKBJ approximation and those from coupled-mode theory. Their condition is derived from a simple assumption that the width of the first Fresnel zone should be much smaller than the scalelength of lateral heterogeneity. This statement has been recognized implicitly since the early stage of the surface wave studies based on geometrical ray theory, and the assumption of smoothly varying heterogeneity around a ray path has been an essential part of ray theory for surface waves (e.g. Woodhouse 1974; Yomogida 1985; Tromp & Dahlen 1992a,b).

One of the ways to overcome the limitations of ray theory is to use scattering theory for surface waves based on the first Born approximation (Snieder 1986, 1987; Yomogida & Aki 1987). For body waves at finite frequency, sensitivity kernels for traveltimes or waveforms have been proposed by many researchers for 2-D cases in the early 1990s based on the scattering theory (Luo & Shuster 1991; Woodward 1992; Yomogida 1992; Vasco & Majer 1993; Li

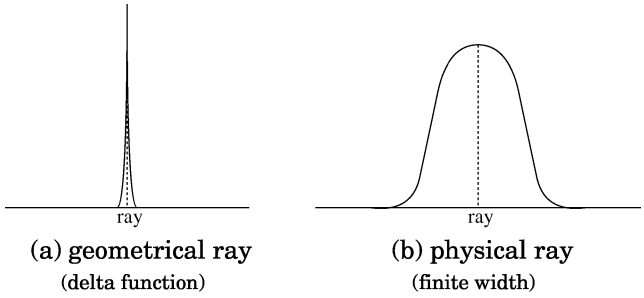

Figure 1. A schematic illustration of the influence zone for: (a) a geometrical ray and (b) a physical ray.

& Tanimoto 1993; Li & Romanowicz 1995; Marquering & Snieder 1995). Such scattering studies have been extended to diffraction studies for 3-D waveform inversion (Meier *et al.* 1997) and to the construction of 3-D sensitivity kernels (Marquering *et al.* 1998, 1999; Dahlen *et al.* 2000; Hung *et al.* 2000; Zhao *et al.* 2000). One of the features of these techniques is that they involve an integral over a finite region, whereas the geometrical ray theory is able to treat the velocity variations only along the ray path. Studies of surface wave scattering based on the Born approximation can be quite useful when local strong heterogeneity exists around a ray path. Although the conditions for the application of such a first-order scattering theory to the real Earth may be rather restrictive.

In geometrical ray theory based on the high-frequency approximation, the influence zone around a surface wave path is supposed to resemble a delta function (Fig. 1). However, actual surface waves with finite frequency should sample a finite region around a ray path. Such a ray with finite width can be termed a physical ray (Červený & Soares 1992). In this paper, we focus on determining the effective width of surface wave rays, which can be defined as the *influence zone* around a surface wave ray path, in which surface wave phases are coherent and there is only constructive interference from scattered waves. As an extension of the ray theory, this zone can be found by considering a bundle of neighbouring rays around a central ray path. We should note that the objective of this paper is to consider a region in which surface waves are coherent and, as a result, we cannot distinguish waves with a slight deviation owing to scattering from a true ray. Thus obtaining rigorous sensitivity kernels is beyond the scope of this study.

In order to investigate the behaviour of rays and to define a particular region surrounding a ray path, we first develop a hybrid ray tracing technique, *Fresnel-area ray tracing* (FRT) for surface waves on a spherical Earth. The concept was originally developed by Červený & Soares (1992) for body waves. The FRT technique consists of two standard ray tracing techniques, kinematic ray tracing (KRT) and dynamic ray tracing (DRT). KRT is used to determine the ray trajectories (geometrical rays) in heterogeneous structures, and DRT provides us with the relative behaviour of neighbouring or paraxial rays. Combining the solutions from KRT and DRT, a paraxial Fresnel area around a ray path can be obtained. In order to trace frequency-dependent surface wave rays in a laterally heterogeneous structure, we need to evaluate surface wave phase speeds at each geographical point, depending on frequency and mode. Therefore, in this study, we restrict our attention to phase-speed structure rather than a 3-D structure, because it is more efficient to work with off-great-circle propagation. FRT makes it possible to construct the stationary-phase field around a ray path (rather than just the great circle) in a laterally heterogeneous structure. The influence zone around a ray path is estimated from the properties of this stationary-phase field.

2 FORMULATION FOR FRESNEL-AREA RAY TRACING

Since the theory and procedure of surface wave ray tracing, especially KRT and DRT, have been well established by the effort of many researchers (e.g. Woodhouse 1974; Jobert & Jobert 1987; Yomogida & Aki 1985; Dahlen & Tromp 1998), we briefly summarize the essence of these standard ray methods. FRT for surface waves on a spherical Earth is then developed by combining the solutions from KRT and DRT.

2.1 Kinematic ray tracing

The KRT equations in a spherical polar coordinate system (θ, ϕ) can be represented as a set of three coupled ordinary differential equations (e.g. Aki & Richards 1980; Dahlen & Tromp 1998),

$$\frac{d\theta}{ds} = \cos\zeta, \tag{1}$$

$$\frac{d\phi}{ds} = \frac{\sin\zeta}{\sin\theta}, \tag{2}$$

$$\frac{d\zeta}{ds} = \sin\zeta\,\partial_\theta \ln c - \frac{\cos\zeta}{\sin\theta}\partial_\phi \ln c - \cot\theta\sin\zeta, \tag{3}$$

where the dependent variable s is the angular distance along a ray path, ζ is the local azimuth that corresponds to the propagation direction of a ray and c is the local phase velocity. The geometrical configuration is displayed in Fig. 2.

When we trace a ray on a spherical Earth, it is convenient to rotate the coordinate system for the source and receiver pairs so that the great circle lies on the equator as seen in Fig. 2. In the rotated spherical coordinate system, the source location is always $(\pi/2, 0)$ and the coordinate of a receiver at the epicentral distance Δ is $(\pi/2, \Delta)$. In this study, all ray tracing is considered in these rotated spherical polar coordinates.

The sets of differential eqs (1)–(3) can be solved numerically with appropriate initial conditions for each equation. In the rotated coordinate system the initial conditions are

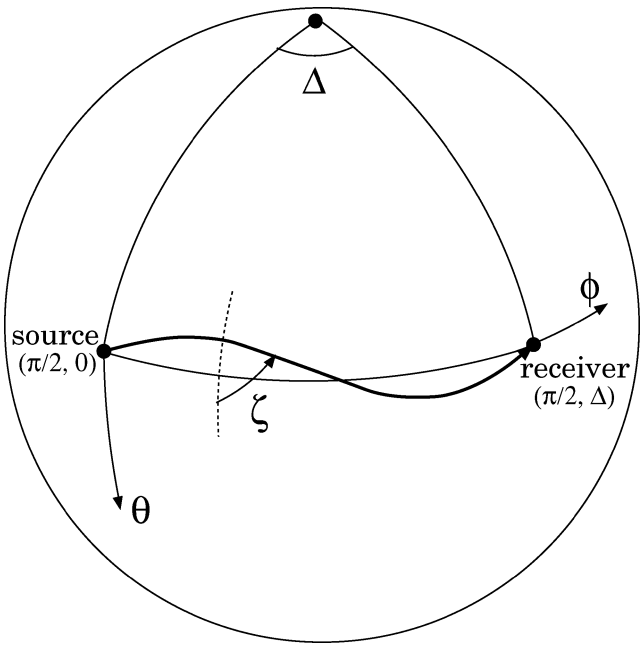

Figure 2. A surface wave ray in a 'rotated' spherical-polar coordinate system where the source and receiver are on the equator. The propagation direction ζ at (θ, ϕ) is measured from the south.

$$\theta(0) = \frac{\pi}{2}, \quad \phi(0) = 0, \quad \zeta(0) = \zeta_0. \tag{4}$$

When we calculate an arbitrary ray path with a certain take off angle ζ' at the source, we do not need to estimate the initial angle and we can just put $\zeta_0 = \zeta'$. For a two-point shooting problem, the initial angle $\zeta_0 = \pi/2 + \delta\zeta$ in the rotated coordinate system can be estimated by ray perturbation theory (Woodhouse & Wong 1986; Dahlen & Tromp 1998). The perturbed initial take-off angle can be found from

$$\delta\zeta = -\frac{1}{c \sin\Delta} \int_0^{\Delta} \sin(\Delta - \phi)\partial_\theta \delta c \, d\phi. \tag{5}$$

The integration in eq. (5) is to be calculated along the great circle. If the lateral heterogeneity is not too strong, the linear relation (5) offers a fairly good estimate for the initial angle. To hit the receiver, we need to solve the set of ray tracing equations iteratively. A practical numerical scheme for solving these equations is provided by iterative use of the Runge–Kutta method.

2.2 Dynamic ray tracing

The kinematic ray tracing systems are useful for tracing an actual ray, but only provide us with ray trajectories. When we are interested in the wavefield surrounding a ray rather than just on a line (or ray trajectory), it is necessary to consider the behaviour of the neighbouring or paraxial rays surrounding the central ray. In order to investigate the relative behaviour of rays, we can obtain dynamic ray tracing equations by differentiating the kinematic ray tracing equations (1)–(3) with respect to the initial take-off angle ζ_0,

$$\frac{d}{ds}\left(\frac{\partial\theta}{\partial\zeta_0}\right) = -\sin\zeta \frac{\partial\zeta}{\partial\zeta_0}, \tag{6}$$

$$\frac{d}{ds}\left(\frac{\partial\phi}{\partial\zeta_0}\right) = -\frac{\cot\theta \sin\zeta}{\sin\theta}\frac{\partial\theta}{\partial\zeta_0} + \frac{\cos\zeta}{\sin\theta}\frac{\partial\zeta}{\partial\zeta_0}, \tag{7}$$

$$\frac{d}{ds}\left(\frac{\partial\zeta}{\partial\zeta_0}\right) = A\frac{\partial\theta}{\partial\zeta_0} + B\frac{\partial\phi}{\partial\zeta_0} + C\frac{\partial\zeta}{\partial\zeta_0}, \tag{8}$$

where

$$A = \sin\zeta\,\partial_\theta^2 \ln c + \frac{1}{\sin\theta}\left[\cot\theta\cos\zeta\,\partial_\phi \ln c - \cos\zeta\,\partial_\theta\partial_\phi \ln c + \frac{\sin\zeta}{\sin\theta}\right], \tag{9}$$

$$B = \sin\zeta\,\partial_\phi\partial_\theta \ln c - \frac{\cos\zeta}{\sin\theta}\partial_\phi^2 \ln c, \tag{10}$$

$$C = \cos\zeta\,\partial_\theta \ln c + \frac{\sin\zeta}{\sin\theta}\partial_\phi \ln c - \cot\theta\cos\zeta. \tag{11}$$

The initial conditions for these three differential equations may be given by assuming a point source,

$$\frac{\partial\theta(0)}{\partial\zeta_0} = 0, \quad \frac{\partial\phi(0)}{\partial\zeta_0} = 0, \quad \frac{\partial\zeta(0)}{\partial\zeta_0} = 1. \tag{12}$$

The geometrical spreading J can be evaluated from the solutions of the DRT equations (6)–(8) as follows (e.g. Yomogida & Aki 1985; Jobert & Jobert 1987):

$$J(s) = \left[\left(\frac{\partial\theta}{\partial\zeta_0}\right)^2 + (\sin\theta)^2\left(\frac{\partial\phi}{\partial\zeta_0}\right)^2\right]^{1/2}. \tag{13}$$

If there exist caustics where neighbouring rays cross then

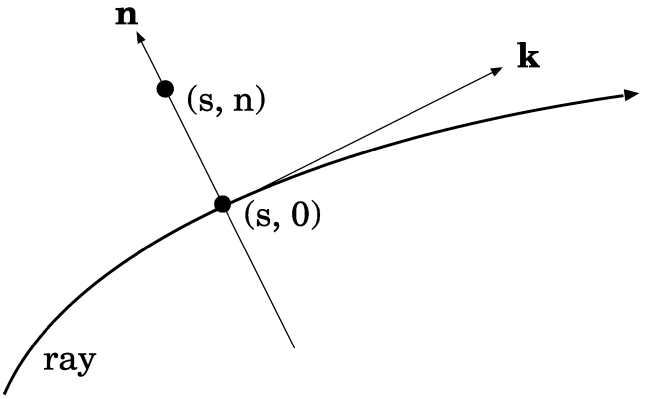

Figure 3. Ray-centred coordinate system. An arbitrary point (s, n) is measured from a point on a central ray $(s, 0)$.

$$\frac{\partial\theta}{\partial\zeta_0} = \frac{\partial\phi}{\partial\zeta_0} = 0, \tag{14}$$

and this condition can be used to determine the locations of caustics.

2.3 Paraxial Fresnel area

Using the results from the KRT and DRT, the Fresnel area surrounding a ray can be estimated based on the paraxial ray theory. The estimated Fresnel area may be called the 'paraxial Fresnel area'. The theory of paraxial ray approximations has been discussed extensively by Červený (e.g. Červený 1985, 1987; Červený *et al.* 1988) for the body wave case and by Yomogida (Yomogida 1985, 1988; Yomogida & Aki 1985) for the surface wave case, working in ray-centred coordinates.

First, let us introduce a ray-centred coordinate system on a spherical surface (s, n): s corresponds to the distance along the ray path, and n is a coordinate perpendicular to the ray path and $n = 0$ on the central ray (Fig. 3). When we expand the phase ψ in a Taylor series around a point on the ray $(s, 0)$ at fixed s,

$$\psi(s, n) = \psi(s, 0) + \frac{1}{2}n^2 M(s), \tag{15}$$

where,

$$M(s) = \left.\frac{\partial^2\psi(s, n)}{\partial n^2}\right|_{n=0} = \frac{\omega}{c(s)J(s)}\frac{dJ(s)}{ds}. \tag{16}$$

See Appendix A for explicit formulations of eqs (15) and (16).

Now let us define the first Fresnel zone surrounding a ray trajectory for a point source at A and a receiver at B (Fig. 4). Introducing a point F near the ray path, the first Fresnel zone is defined in terms of the phase behaviour as follows:

$$\left|\psi_A^F + \psi_B^F - \psi_A^B\right| \le \pi, \tag{17}$$

where ψ_A^F, ψ_B^F and ψ_A^B are the phases integrated along ray paths A–F, B–F and A–B. Considering the points F at (s, n) and O_F at $(s, 0)$, the phases ψ_A^F and ψ_B^F can be obtained from eq. (15),

$$\psi_A^F = \psi_A^{O_F} + \frac{1}{2}n^2 M_A^{O_F}, \tag{18}$$

$$\psi_B^F = \psi_B^{O_F} + \frac{1}{2}n^2 M_B^{O_F}. \tag{19}$$

Both eqs (18) and (19) are defined along the same ray trajectory, but in different ray-centred coordinate systems. That is, the coordinate

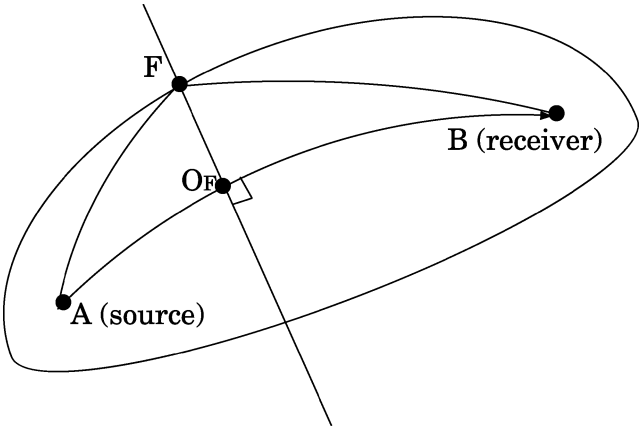

Figure 4. Schematic view of the Fresnel area around a ray. The radius of Fresnel zone is defined by the line F–O_F.

system of eq. (18) is (s, n), whilst eq. (19) is $(\Delta - s, n)$, where Δ is the distance from source to receiver along the ray path. Using the relation $\psi_A^{O_F} + \psi_B^{O_F} = \psi_A^B$, and substituting eqs (18) and (19) into eq. (17), the equation for the paraxial Fresnel area can be obtained,

$$\frac{1}{2}n^2 \left| M_A^{O_F} + M_B^{O_F} \right| \leq \pi. \tag{20}$$

We can finally obtain the radius of the paraxial Fresnel area measured from the ray path,

$$n = \left(\frac{2\pi}{\left| M_A^{O_F} + M_B^{O_F} \right|} \right)^{1/2}, \tag{21}$$

where $M_A^{O_F}$ and $M_B^{O_F}$ can be expressed as

$$M_A^{O_F} = \frac{\omega}{c(O_F)} \frac{J_A'(O_F)}{J_A(O_F)}, \quad M_B^{O_F} = \frac{\omega}{c(O_F)} \frac{J_B'(O_F)}{J_B(O_F)}, \tag{22}$$

with $J' = dJ/ds$. On inserting eq. (22) into eq. (21), the final form for the radius of the paraxial Fresnel area can be expressed as

$$n = \left(\frac{2\pi c}{\omega} K \right)^{1/2} = (TcK)^{1/2} = (\lambda K)^{1/2}, \tag{23}$$

where T is the period of the wave, λ is a wavelength and $K = J_A J_B / |J_A' J_B + J_B' J_A|$. At caustic points, the geometrical spreading J shrinks to 0, and thus the radius of the paraxial Fresnel area is also 0. Since the radius of the exact Fresnel area at the point source is very close to $\lambda/2$ in the case of the first Fresnel zone (see Appendix B), we may therefore expect a radius of the Fresnel zone of the same order of $\lambda/2$ even at caustics.

3 SYNTHETIC TESTS OF FRESNEL-AREA RAY TRACING

In order to check the validity of the formulation and behaviour of Fresnel zones in laterally heterogeneous structure, examples of paraxial Fresnel areas in synthetic models are displayed in this section.

3.1 Comparison with the exact and the paraxial Fresnel area

The exact Fresnel area can simply be calculated for a laterally homogeneous structure since we can compute the traveltime along a great circle without any ray tracing. Let us consider the geometrical configuration in the rotated spherical polar coordinates as shown in Fig. 5. The definition of the first Fresnel zone, with respect to the path-length, can be written as

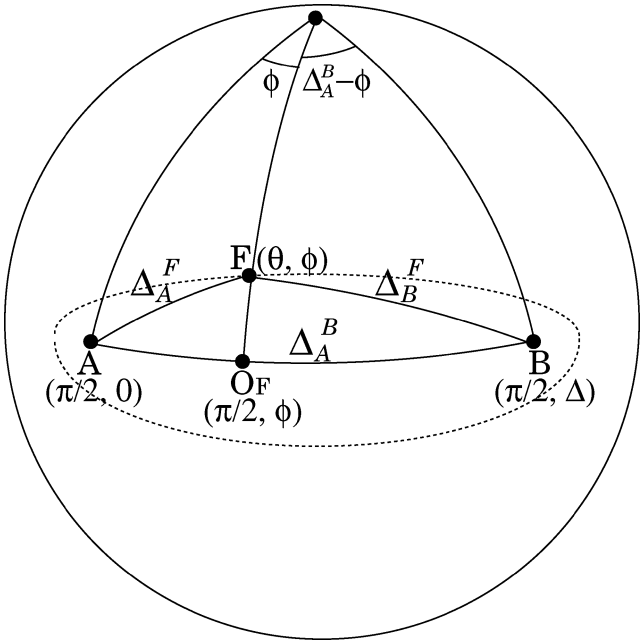

Figure 5. Illustration of an exact Fresnel area on a spherical surface in a rotated spherical-polar coordinate system.

$$\left| \Delta_A^F + \Delta_B^F - \Delta_A^B \right| \leq \frac{\lambda}{2}, \tag{24}$$

which provides an alternative form to eq. (17). Δ_A^B is the epicentral distance and the arclengths Δ_A^F and Δ_B^F can be expressed in terms of spherical trigonometry,

$$\cos \Delta_A^F = \cos \frac{\pi}{2} \cos\theta + \sin \frac{\pi}{2} \sin\theta \cos\phi = \sin\theta \cos\phi, \tag{25}$$

$$\cos \Delta_B^F = \cos \frac{\pi}{2} \cos\theta + \sin \frac{\pi}{2} \sin\theta \cos\left(\Delta_A^B - \phi\right) = \sin\theta \cos\left(\Delta_A^B - \phi\right). \tag{26}$$

The boundaries of the exact Fresnel area on the spherical surface can be obtained by solving eqs (24)–(26) numerically.

Examples of the exact Fresnel area and the paraxial Fresnel area in a laterally homogeneous structure for three different periods (25, 40, 100 s) are shown in Fig. 6(a). We can see that the paraxial Fresnel area is a fairly good approximation of the exact one, except close to the source and receiver positions where the geometrical spreading shrinks to 0 and, as a result, the paraxial Fresnel area vanishes. As the period increases, the agreement between the exact and the approximate Fresnel area becomes worse. As mentioned at the end of the previous section, we may rectify the problem by assuming that the paraxial Fresnel area at the source and the receiver as well as at any possible caustic point have a Fresnel area radius of the order of $\lambda/2$ for the first Fresnel zone. Paraxial Fresnel areas with corrections at the source and the receiver are shown in Fig. 6(b). Such corrections are quite useful for matching the paraxial Fresnel areas and the exact ones for an even longer period. The detailed procedure for the correction of the paraxial Fresnel area is explained in Appendix B.

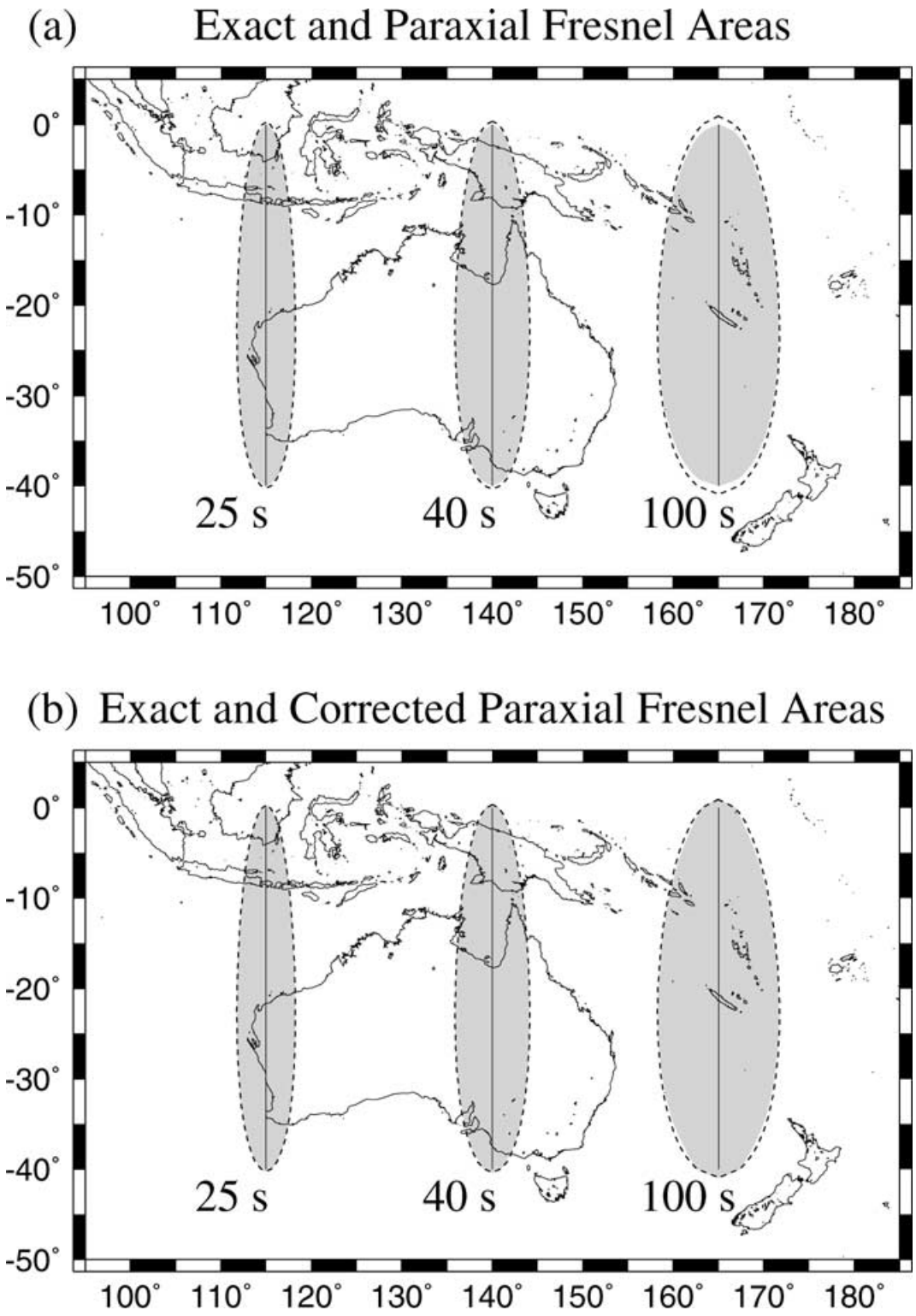

Figure 6. (a) Exact (solid ellipsoid) and paraxial (shaded ellipsoid) Fresnel areas at 25 (left), 40 (middle) and 100 (right) s. The background map is only plotted for the measure of the scale. (b) Same as in (a) but for paraxial Fresnel areas with corrections at the source and the receiver.

3.2 Hotspot heterogeneity

We next perform synthetic tests with simple hotspot models (Fig. 7). These models contain a circular region with a radius of 4° and the Rayleigh wave phase velocity is 10 per cent slower than the surrounding area. These tests give us an insight into how the location of a strong heterogeneity affects the wavefield and the Fresnel area around a ray.

As can be clearly seen in Fig. 7, if the source is adjacent to a strongly heterogeneous region, ray paths that are radiated toward the heterogeneity are distorted significantly. When the source lies slightly away from the heterogeneity but is still close enough, we can

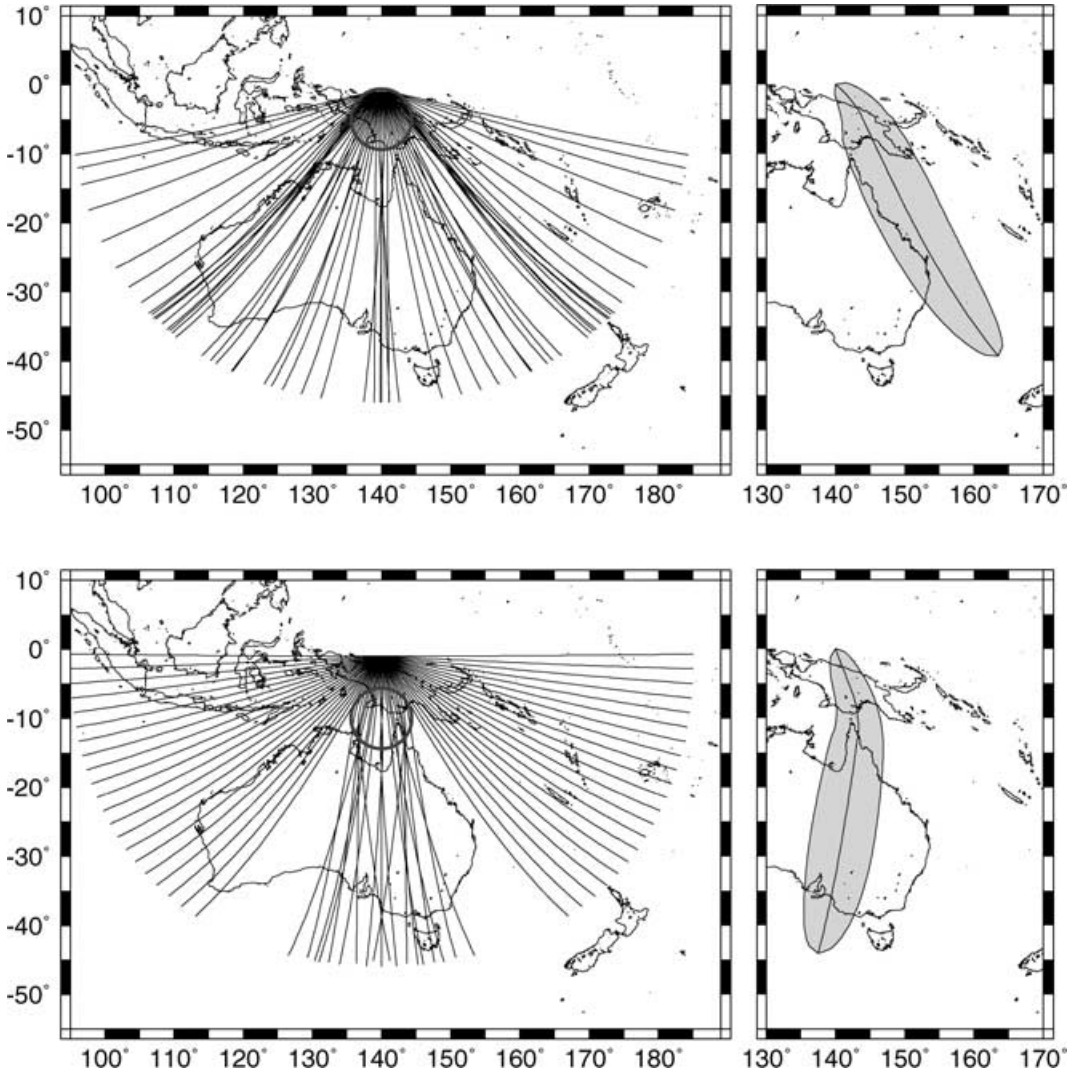

Figure 7. Ray paths in hotspot models (left) and corresponding paraxial Fresnel areas for 40 s (right). Both regions inside and outside the circle are homogeneous, but the Rayleigh wave phase velocity inside the circle is 10 per cent slower than the outside. The locations of the hotspot are 5°S, 140°E (top) and 10°S, 140°E (bottom). The source location is 1°S, 140°E for both case. The distances from sources to the centre of the circle are 4° (top) and 9° (bottom). Rays are radiated with the azimuths from 90° to 270° for every 3°.

see areas of focusing and defocusing behind the circular heterogeneity. The Fresnel areas shown for each heterogeneity configuration suggest that they are severely affected by the strong velocity gradient in the vicinity of the heterogeneity and, as a result, the radii of the Fresnel zone becomes smaller in such regions because the ray path density is very high, in other words, the surface wave energy concentrates in that particular area.

We should note here that, with a ray-based technique such as that used in this study, we cannot treat the full range of complex multipath effects which can be caused in the presence of a strong lateral heterogeneity such as this hotspot model, although such rapid and strong velocity variations are not seen in most phase-speed models.

4 INFLUENCE ZONE INFERRED FROM STATIONARY-PHASE FIELD

In the previous section, we have shown the estimates of the first Fresnel zones obtained from FRT. Now we examine the nature of the variation around surface wave paths as an extension of the geometrical ray theory using stationary-phase fields.

4.1 Stationary-phase field

Using FRT, stationary phases around surface wave ray paths in laterally heterogeneous structure can be evaluated simply. First, let us define a reference waveform U_0 along a central ray for a frequency ω as

$$U_0(\omega) = A_0(\omega) \exp[-i\psi_0(\omega)], \tag{27}$$

where the complex amplitude term A_0 contains the source radiation, the receiver eigenfunction, geometrical spreading and the spatial variation of amplitude caused by a background structure, ψ_0 is the phase of the wave integrated along the ray. Explicit forms for A_0 can be found in many textbooks (e.g. Aki & Richards 1980; Kennett 1983; Dahlen & Tromp 1998). As in most surface wave studies, the wavefield U_0 along a ray path can be calculated as a WKBJ seismogram. Hereafter we abbreviate the notation for the frequency dependence.

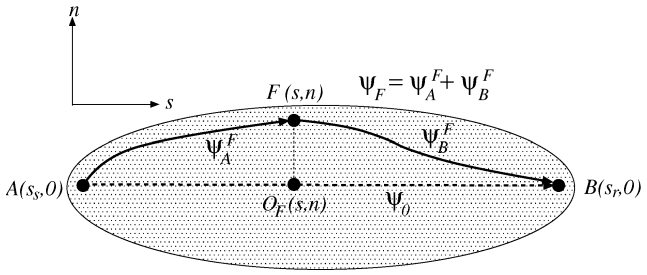

Figure 8. Geometrical configuration of influence zone (shaded area), a geometrical ray (AO_F B) and a perturbed ray (AFB).

Now let us assume that the waveforms along perturbed rays that arrive at a receiver passing through a point $F(s, n)$ near the central ray (Fig. 8) can be written as

$$U_F = A_F \exp(-i\psi_F), \tag{28}$$

where A_F is a perturbed amplitude term for the off-centre ray path and $\psi_F = \psi_A^F + \psi_B^F$ is a perturbed phase term integrated along the path. U_F represents the perturbed wave and is to be distinguished from scattered or diffracted waves for which an inclination factor and different geometrical spreading need to be considered (e.g. Born & Wolf 1999). From eq. (20), the perturbation of phase between a central ray and neighbouring rays can be expressed as

$$\delta\psi_F = \psi_F - \psi_0 = \frac{1}{2}n^2 M_F(s), \tag{29}$$

where $M_F(s) = |M_A^{O_F}(s) + M_B^{O_F}(s)|$ is derived from FRT. Substituting eq. (29) into eq. (28) and using eq. (27), we obtain a relation between U_F and U_0,

$$U_F = A_F \exp(-i\psi_0)\exp(-i\delta\psi_F) \tag{30}$$

$$= \frac{A_F}{A_0} U_0 \exp(-i\delta\psi_F). \tag{31}$$

The exponential term in eq. (31) depends only on the background structure, and we can therefore estimate the stationary-phase field around a central ray path by evaluating this term.

To investigate the behaviour of the phase term in eq. (31), let us consider an explosive source for which the azimuthally dependent radiation effect can be ignored, and assume that amplitude variation in the background structure is smooth and differences of epicentral distance along a central ray and along perturbed rays are small enough so that the differences in geometrical spreading can be ignored. In such circumstances, we can assume that $A_F \approx A_0$ near the central ray path, and the perturbed waveform can be represented as

$$U_F \approx U_0 \exp(-i\delta\psi_F) = U_0 \exp\left(-\frac{i}{2}n^2 M_F\right). \tag{32}$$

An example of the stationary-phase function $\exp(-\frac{1}{2}in^2 M_F)$ for ray paths to CAN and NWAO stations is given in Fig. 9(a). Surface wave rays are traced on a 40 s Rayleigh wave phase-speed model obtained from a 3-D Australian Continent model of Debayle & Kennett (2000). Throughout this study, this 3-D model is used to reconstruct 2-D phase-speed maps. Crustal corrections for these phase-speed maps are made by using the 3SMAC model (Nataf & Ricard 1996). Contours around each ray path correspond to the Fresnel zones, and up to the eighth Fresnel zone is shown in this example.

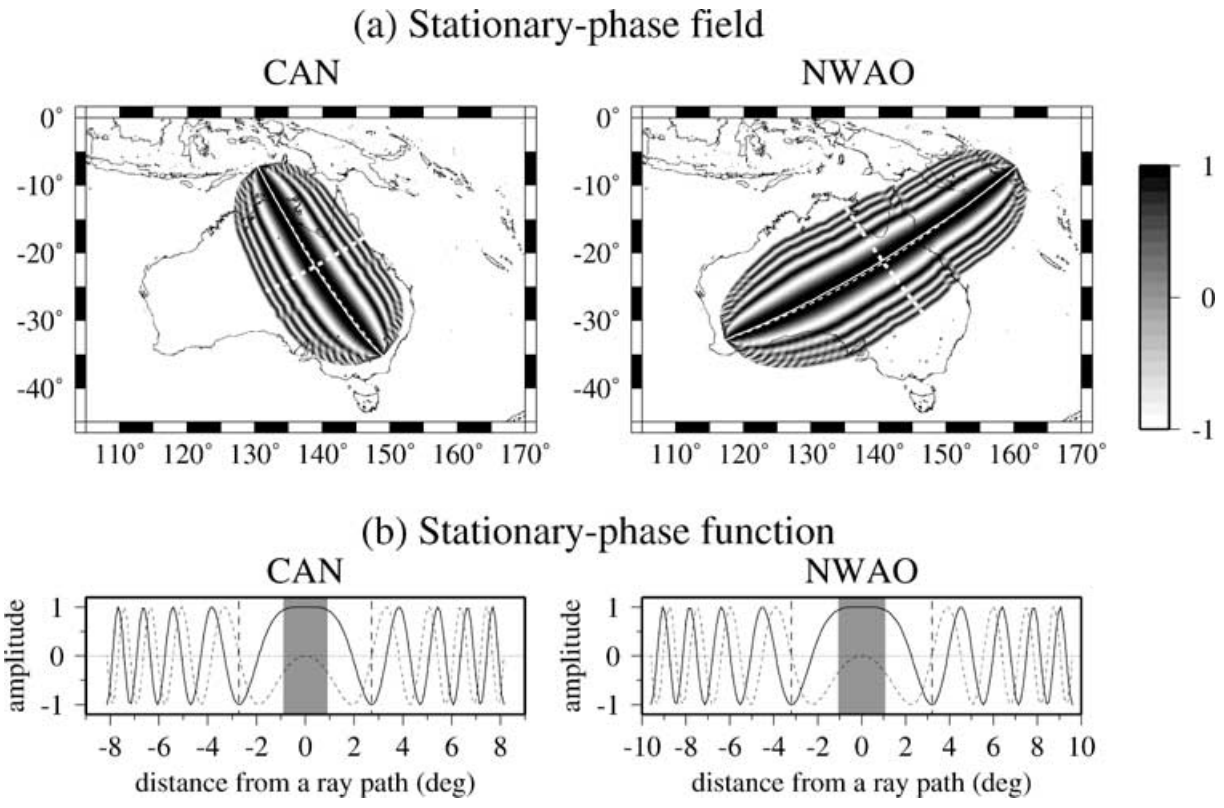

Figure 9. (a) Spatial projections of the real part of the stationary-phase function for CAN and NWAO stations. White solid lines denote geometrical rays and white dotted lines denote corresponding great circle. Rays are traced on a 40 s Rayleigh wave phase-speed map. (b) Cross-section of stationary-phase field along white thick-dotted lines in (a). Solid lines denote the real part of the stationary-phase function and dashed lines denote the imaginary part. Vertical dashed lines show the first Fresnel zone and shaded areas show 1/3-width of the first Fresnel zone.

The cross-sections of the phase function of both real and imaginary parts at the middle of the source–receiver distance are shown in Fig. 9(b). This type of function around a ray path has previously been presented in the context of Born scattering (Aki & Richards 1980; Yomogida 1992; Marquering *et al.* 1998). Yomogida (1992) obtained Fréchet kernels, which have a similar character to the phase functions shown here, considering Fresnel zones around a ray path for body wave case. Marquering *et al.* (1998) used the phase function for a discussion of the validity of the stationary-phase approximation. Note the definition of the Fresnel zone implicitly includes a first-order Born approximation. However, it should be emphasized that our objective is not to try to discuss rigorous sensitivity kernels considering scattering or diffraction, but to focus on the determination of a region around the geometrical ray path for surface waves, in which the surface wave phases can be regarded as coherent, since we wish to understand the scattering region appropriate to surface wave tomography.

4.2 Extended influence zone

In geometrical ray theoheory, the waveform U_0 is evaluated along a ray (or a great circle). Thus the influence zone for U_0 is supposed to be just like a delta function on the ray (Fig. 1). We now take a different viewpoint from traditional ray theory to extend the effective zone for the surface wavefield. We want to find the region about the ray (the *influence zone*) in which the wavefield is coherent. An average wavefield $U_{\rm av}$ over a zone Σ can be defined as

$$U_{\rm av} \equiv \frac{\iint_\Sigma U_{\rm F}(s_r, 0; s, n)\, ds\, dn}{\iint_\Sigma ds\, dn}, \tag{33}$$

where Σ is an area around the ray on the spherical surface and $U_{\rm F}(s_r, 0; s, n)$ is the waveform along a path which passes through a point (s, n) and reaches the receiver $(s_r, 0)$ (Fig. 8). Using the paraxial approximation eq. (32), the average wavefield can be expressed as

$$U_{\rm av} \approx U_0 \frac{\iint_\Sigma \exp(-i\delta\psi_{\rm F})\, ds\, dn}{\iint_\Sigma ds\, dn}. \tag{34}$$

Thus if we require the average wavefield $U_{\rm av}$ to be approximately equal to U_0, we require the average to be taken over an influence zone Σ_I such that,

$$\frac{\iint_{\Sigma_I} \exp(-i\delta\psi_{\rm F})\, ds\, dn}{\iint_{\Sigma_I} ds\, dn} \approx 1. \tag{35}$$

Eq. (35) leads us to a necessary and sufficient condition for the influence zone,

$$\exp(-i\delta\psi_{\rm F}) = \exp\left[-\frac{i}{2}n^2 M_{\rm F}(s)\right] \approx 1. \tag{36}$$

It is clear that eq. (36) is sufficient to satisfy eq. (35). The necessity of condition (36) arises from the fact that the denominator in eq. (35) is a monotonically increasing real function, whereas the numerator is a complex function that is oscillating along the n-direction. It may be worth noting that the range of the n-integration should not be too far away from the central ray, because we have assumed that both the spatial amplitude variation and the differences of epicentral distances between rays should be small in the region under consideration (see eq. 32). Note that condition (36) is also valid for the geometrical ray theory in which n-integration in eq. (34) is simply evaluated just on the central ray, that is, $n = 0$; this satisfies condition (36) exactly, i.e. $\exp(-i0) = 1$.

The influence zone for the surface wave paths, which satisfies the necessary and sufficient condition (36), can be readily found from a diagram of the stationary-phase function (Fig. 9b). We can recognize a fairly flat area around a central ray ($n = 0$) in the real part of the phase function, whilst the imaginary part is close to zero. Now we will focus on this region to determine the influence zone. For this purpose, we use the condition for wavefield coherence in an integral form, eq. (35), to investigate the zone that may have significant effects on the total wavefield. Condition (35) can be rewritten using eq. (29) as

$$I(n_I) = \frac{\int_0^\Delta \int_{-n_I W(s)}^{n_I W(s)} \exp[-i/2n^2 M(s)]\, dn\, ds}{\int_0^\Delta \int_{-n_I W(s)}^{n_I W(s)} dn\, ds} \approx 1, \tag{37}$$

where Δ is a ray length, $W(s)$ is a half-width of the first Fresnel zone at a point s on the central ray, and n_I is a coefficient for determining the width of a region to be integrated. n_I is normalized to be 1.0 for the first Fresnel zone. Considering the real and imaginary parts of $I(n_I)$, the condition (37) can be reformed as

$$\mathrm{Re}\{I(n_I)\} \approx 1 \quad \mathrm{Im}\{I(n_I)\} \approx 0. \tag{38}$$

Fig. 10 shows diagrams of the real and imaginary parts of $I(n_I)$ as a function of the normalized coefficient n_I. The criteria can be satisfied exactly only at the central ray path. We, therefore, need to set threshold values that satisfy eq. (38) reasonably well such as

$$\mathrm{Re}\{I(n_I)\} \geq 0.9 \quad |\mathrm{Im}\{I(n_I)\}| \leq 0.1. \tag{39}$$

At the 1/3-width of the first Fresnel zone (i.e. $n_I = 1/3$), we find that $\mathrm{Re}\{I(n_I)\} \approx 0.98$ and $|\mathrm{Im}\{I(n_I)\}| \approx 0.1$ (Fig. 10), which satisfies the condition (39). This area can be regarded as the *influence zone* over which the perturbed waveforms are fairly coherent in phase; giving a constructive interference for surface wavefields within the influence zone, whilst outside there is rather a destructive interference caused by the rapid fluctuation of the phase function, as shown in Fig. 9(b).

Since the width of the Fresnel zone is proportional to the square root of the phase differences between the central ray path and a neighbouring ray path (see eq. 21), the condition on the size of the influence zone can be written in a similar form to eq. (17),

$$|\delta\psi_{\rm F}| = \left|\psi_{\rm A}^{\rm F} + \psi_{\rm B}^{\rm F} - \psi_{\rm A}^{\rm B}\right| \leq \frac{\pi}{9}. \tag{40}$$

The choice of the 1/3-width of the first Fresnel zone as the *influence zone* may seem to be somewhat arbitrary, but this is a reasonable choice as discussed in the following section in the context of the uncertainties in actual phase-speed measurements.

We should recall that the paraxial Fresnel zone shrinks to 0 at the source, receiver and caustic points. However, the radius of the first Fresnel zone at these points are approximately $\lambda/2$. Thus the radius of the influence zone at the source and the receiver is expected to be $\lambda/6$. A similar argument may be applied along the path and the influence zone can be extended slightly beyond the positions of source and receiver (see Appendix B).

Examples of the *influence zones* for the ray paths in Fig. 9(a) are shown in Fig. 11 for fundamental-mode Rayleigh waves at 40 and 100 s. The width of the physical rays become wider for longer period waves, because the width of the Fresnel zone is proportional to the square-root of the product of the phase velocity and the period of the waves as shown in eq. (23). In Fig. 12, physical rays for both the fundamental and the first higher-mode Rayleigh waves at 40 s are displayed. These rays pass through a region with moderate (not smooth) heterogeneities near the continent–ocean boundary in eastern Australia. For the fundamental mode, the great circle between

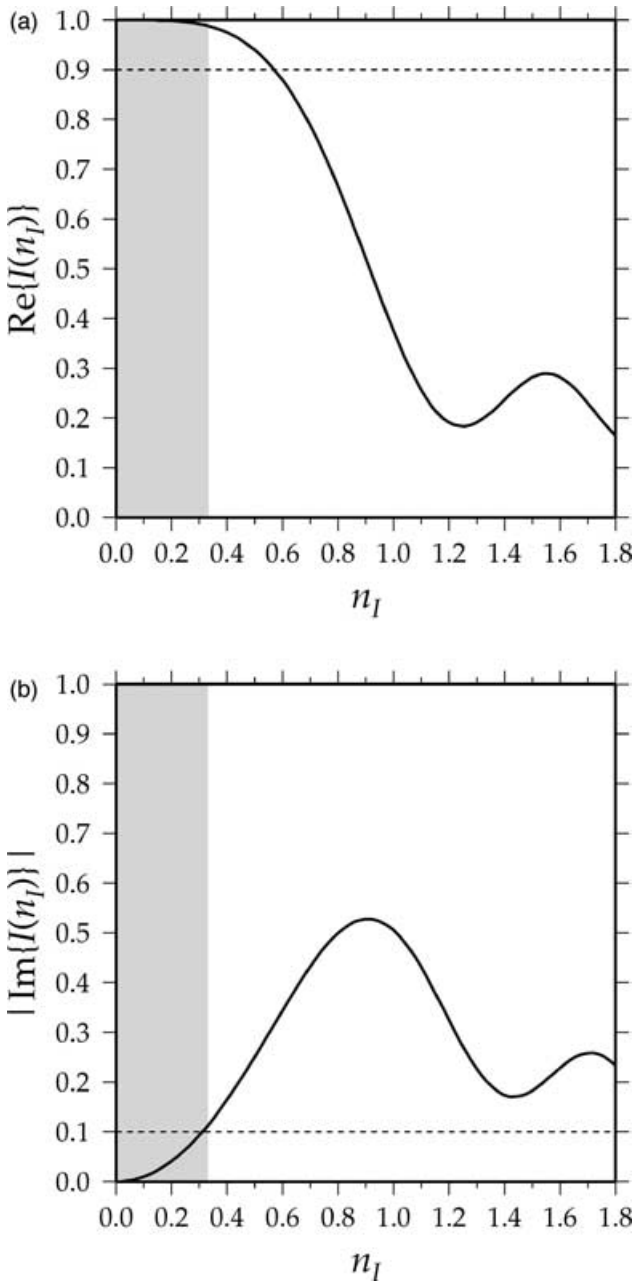

Figure 10. (a) Real part of an integral function $I(n_I)$ as a function of coefficients for a distance from the central ray path n_I. Note that n_I is normalized so that n_I becomes 1 at the first Fresnel zone. (b) Same as in (a) but for the imaginary part of $I(n_I)$. Lateral dashed lines show the criteria for the influence zone (see eq. 39) and shaded areas show 1/3-width of the first Fresnel zone ($n_I = 1/3$).

the source and the receiver grazes along the edge of the influence zone, whilst the ray for the first higher mode passes the other side of the great circle. In such a case, we will need to take into account both the different influence zones as well as the different ray paths for each mode. Such effects cannot be treated with the traditional geometrical ray theory and with the great-circle approximation. Thus, physical rays in phase-speed structures provide us with the possibility of enhancing the current methods of surface wave analysis, even with moderate lateral heterogeneity for which geometrical ray theory and the approximation of wave propagation along the great circle tend to breakdown.

4.3 Evaluation of the influence zone

We now discuss the nature of the influence zone defined in the previous section. First, let us look at the stationary-phase function in the time domain as a function of distance from a ray. Fig. 13 displays the phase function in the time domain with a narrow-frequency band around 25 mHz (40 s) at $n_I = 0$, $\frac{1}{3}$ and 1 (where $n_I = 1$ corresponds to the half-width of the first Fresnel zone). The phase function at $n_I = \frac{1}{3}$ is quite coherent with that at $n_I = 0$ with only a very slight phase shift. This small phase shift is equivalent to the maximum differences in arrival time of a wave along a central ray and that along a neighbouring ray within the influence zone. The arrival-time delay within the influence zone can be estimated analytically. The width of the Fresnel zone is proportional to the square root of the period T of the wave (see eq. 23), so that the 1/3 width of the first Fresnel zone depends on 1/9 of the period. Since the first Fresnel zone is defined as the half-period zone, the arrival-time delay $\delta\tau$ for the influence zone can be estimated as $\frac{1}{2}T \times (\frac{1}{3})^2 = \frac{1}{18}T$, which is equivalent to around 5.6 per cent of the period T. For 40 s surface waves, $\delta\tau \approx 2.2$ s.

As we have explained in the previous section, the surface wavefields within the influence zone are assumed to be coherent. In other words, we cannot distinguish surface waves along different paths that are passing inside the influence zone. However, phase coherence tends to be violated as the perpendicular distance from the central ray becomes large. This effect can be investigated considering the differences in a path-average phase speed along the central path and that along a neighbouring path near the edge of the influence zone as follows. Let us consider the phase of a surface wave along the central ray, $\omega X/\hat{c}$, and that along a neighbouring ray, $\omega(X + \delta X)/(\hat{c} + \delta\hat{c})$, where X and $\hat{c}$ are the ray length along the central ray and the corresponding path-average phase speed, respectively. δX and $\delta\hat{c}$ are the differences in ray length and in path-average phase speeds between the central and neighbouring rays. Here, we ignore the effect of the initial phase from the source and only consider the propagation effect on the phase, assuming that these phase along different rays within the influence zone is coherent and approximately identical,

$$\frac{\omega X}{\hat{c}} \approx \frac{\omega(X + \delta X)}{\hat{c} + \delta\hat{c}}. \tag{41}$$

If we put $\delta\hat{c} = \varepsilon\hat{c}$, where ε is a small parameter, which corresponds to an uncertainty in the perturbation of the path-average phase speeds along different ray paths, then, ε can be represented as

$$\varepsilon = \frac{\delta\hat{c}}{\hat{c}} \approx \frac{\delta X}{X}. \tag{42}$$

For our definition of the influence zone, $\delta X = \frac{1}{2}\lambda(\frac{1}{3})^2 = \frac{1}{18}\lambda$. Now, let us think about Rayleigh waves at 40 s, for which the phase velocity is around 3.9 km s^{-1}. A typical epicentral distance in regional tomography is around 3000 km. In this case, from eq. (42), the difference in the average phase velocity along a central ray and that along a neighbouring ray near the edge of the influence zone is less than 0.3 per cent of the phase velocity. This value is equivalent to or less than the errors in measured phase speeds, which supports the validity of the phase coherence within the influence zone. Note that the estimated errors of phase speeds from eq. (42) become large for longer periods, because it is proportional to the wavelength. Therefore, the coherence in phase within the influence zone becomes worse for longer periods.

The above argument for the validity of the phase coherence also raises a very important aspect of phase-speed measurements at finite frequency. The phase speeds of surface waves are generally measured along the great-circle paths and inevitably have some error in

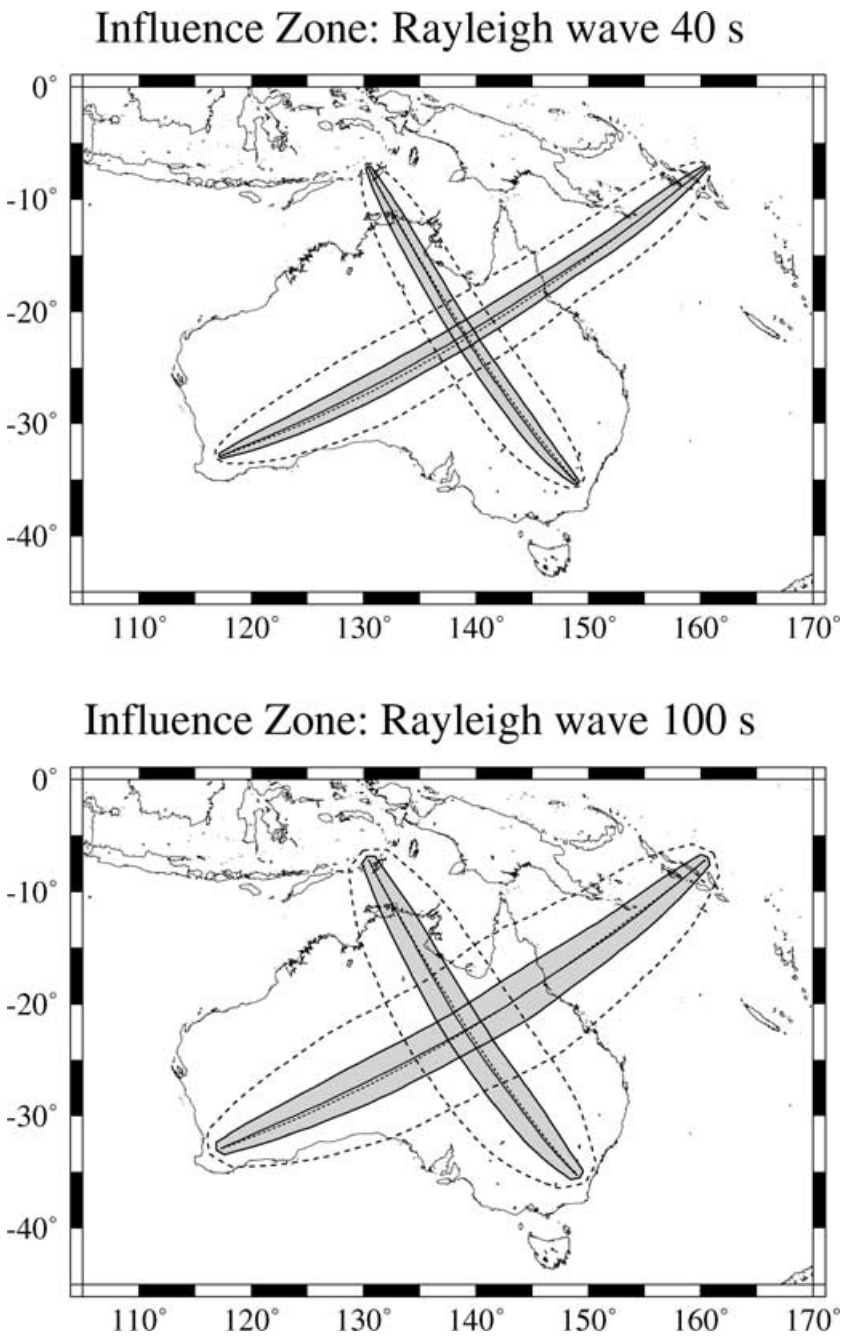

Figure 11. Physical rays of the fundamental-mode Rayleigh waves for two paths to CAN and NWAO stations at 40 s (top) and 100 s (bottom) with correction at the source and receiver. Shaded elliptical areas show the influence zone, dashed ellipsoid show the first Fresnel area and dotted lines show corresponding great circle.

measurement. As we have seen, the apparent phase-speed changes in eq. (42) introduced by deviations in the ray path within the influence zone will generally be less than the errors in phase-speed measurement. For lower-frequency surface waves we can therefore regard the measured phase speeds as an average over the influence zone, rather than an average along the great circle (or the appropriate ray).

Within the influence zone we cannot distinguish scattered waves from bent rays because they have such a similar phase. We can therefore treat the entire influence zone as being equivalent when inverting for phase-speed maps, and employ an area average of the surface wave phase over the influence zone. Because this zone is chosen so that there is very little variation in phase, we do not need to employ a rigorous calculation of the sensitivity kernels, which gives considerable computational savings.

However, outside the influence zone the phases are not coherent. Once we include such paths we need to employ full sensitivity kernels around the central ray paths to accommodate the effects of scattering and diffraction. Such sensitivity kernels for phase-speed structures are discussed in more detail in a future publication.

The *influence zone* defined in the previous section is based on a number of assumptions. However, we can justify the validity of these assumptions in the following way. Since the influence zone is not

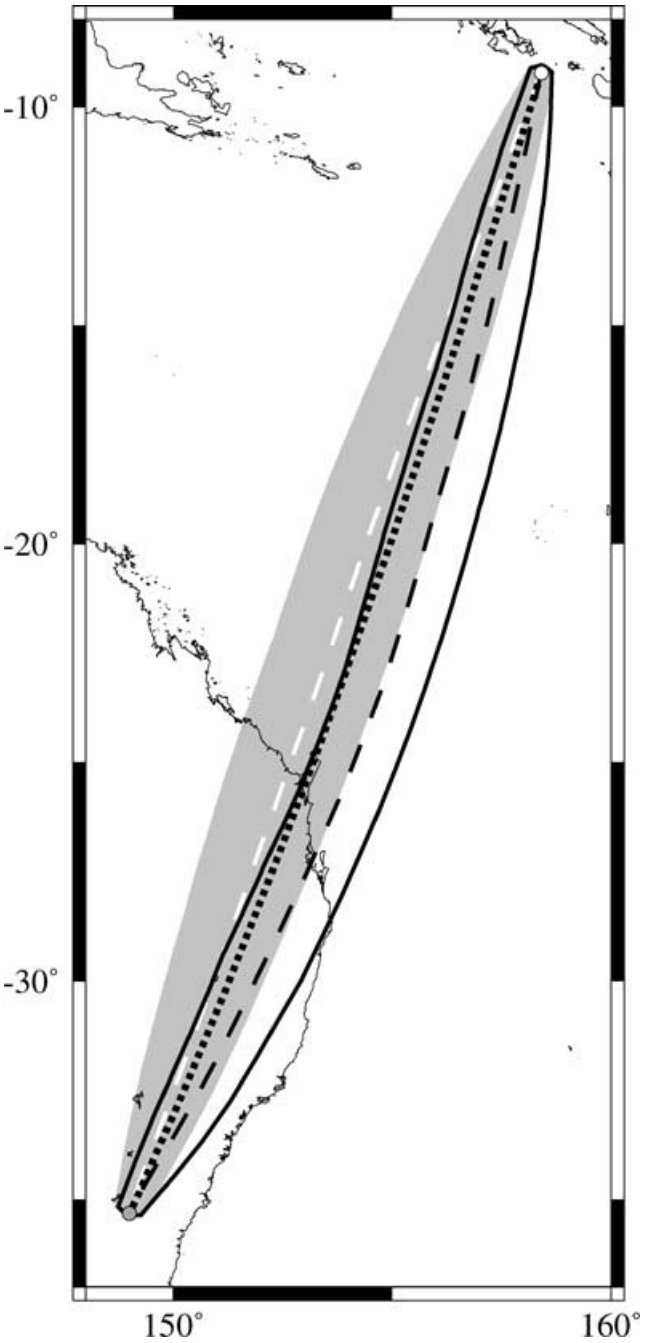

Figure 12. Physical rays of the fundamental mode (black solid ellipsoid) and the first-higher mode (grey-shaded ellipsoid) to CAN station. Corrections are applied at the source and receiver locations. Geometrical rays of these paths are shown in black (the fundamental mode) and white (the first-higher mode) dashed lines. Rays are traced on a 40 s Rayleigh wave phase-speed model. A black dotted line shows the corresponding great circle.

too wide and lies close to the central ray (Fig. 11), the azimuthally dependent radiation effects from a double-couple source may be ignored in a good approximation, except near a nodal direction. The small width of the influence zone also helps to justify the assumption of small spatial amplitude variation and also that of small changes in epicentral distances between rays in the zone. We should note that these assumptions become worse as the period of waves becomes longer and as the mode-branch number increases, because the width of the influence zone becomes wider for these waves.

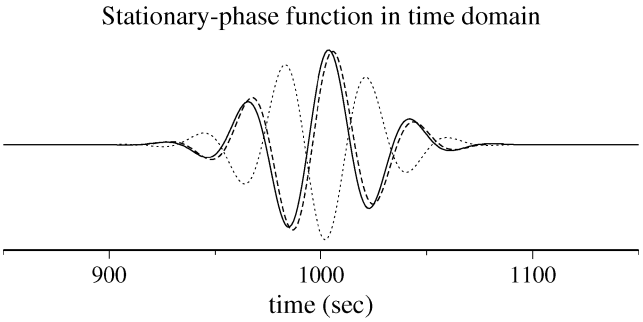

Figure 13. Inverse Fourier-transformed stationary-phase function with a narrow-frequency band around 40 s. The phase function in time domain at $n = 0$ is shown as a solid line, that at $n = 1/3n_1$, where n_1 is the radius of the first Fresnel zone, as a dashed line and that at $n = n_1$ by a dotted line.

The finite-width rays can also be used to estimate the limits on lateral resolution in surface wave tomography. The typical width of physical rays for a 40 s Rayleigh wave with epicentral distances of 3000 km is around 200 km. If two physical rays crossover, the diagonal spread of the crossover region should be slightly larger than the width of the influence zone of the rays (Fig. 11). The estimated lateral resolution for regional surface wave tomography is around 300 km (e.g. Debayle & Kennett 2000). Therefore, the scale of lateral resolution of the tomography is fairly consistent with that of the width of the physical rays, indicating the utility of the concept of the influence zone.

5 DISCUSSION

By using the FRT technique, we have defined the influence zone for surface waves by considering a bundle of neighbouring rays around a ray path. Our definition of the influence zone is that surface waves are coherent in phase within the zone, which implies that the scattered energy within this zone affects the total surface wavefield in a constructive way. The estimated width of the influence zone is approximately one-third of that of the first Fresnel zone.

The influence zone for surface waves defined in this study can be applied simply in 2-D phase-speed inversions. In such a case, the phase speeds measured from observations are no longer just a 'path average', but can be regarded as an 'area average' within the influence zone. From the perspective of finding a realistic Earth model, the difference will be a slight blurring of the phase-speed maps. The use of the physical rays is more appropriate than the use of geometrical rays, in that the realistic finite-frequency effect of wave propagation can be taken into account in tomographic inversion. Vasco *et al.* (1995) have applied simple Fresnel volumes for body waves (corresponding to a Fresnel 'area' for surface waves) using a similar technique to this study based on the method of Červený & Soares (1992). They have shown that tomographic inversions with the Fresnel volumes provide comparable models to those obtained using rigorous sensitivity kernels, which requires considerably more numerical computation.

In most studies of 2-D and 3-D sensitivity kernels, there are prominent variations in sensitivities along the path, that is, the maximum sensitivities appear in the vicinity of the source and receiver. Vasco *et al.* (1995) have also suggested that such variations of the sensitivity along the path can be considered by normalizing the Fresnel volume by its elliptical cross-section area perpendicular to the path (corresponding to the width of the Fresnel area in the 2-D case). This results in a sensitivity peaked at the source and

receiver locations. Such an approach can also be applied to the influence zone in this study, when we apply it to inversions for phase-speed maps, and provides a means of coping with errors in source location. If locations and neighbouring structure of the source and receiver are fixed, there are then strong latent contributions from the sensitivity kernel, but these do not influence the actual results.

In the application of the influence zone to surface wave tomography, it may be worth applying a weight function perpendicular to the central ray to reduce the errors arising from the slightly larger phase differences near the edge of the influence zone. If scattering effects are conspicuous in the observed waveforms and we need to consider scattering effects outside the influence zone, some rigorous calculations for sensitivity kernels will be necessary to take into account the complex effects of scattering and diffraction, which may interfere rather destructively with the total wavefield. As long as we are working with intermediate period waves (say longer than 40 s), strong scattering effects are not expected in the real Earth. However, as the period of interest becomes shorter, we may need to consider the effects of scattering or coupling between mode branches (e.g. Kennett 1984; Kennett & Nolet 1990; Marquering *et al.* 1999).

One of the significant advantages of the FRT technique is that off-great-circle propagation can be treated effectively. Since the width of the Fresnel zone around a ray path depends on the phase-velocity gradient, which is evaluated on the central ray, the influence zone should be obtained around an actual ray rather than around a great circle. However, this may not be critical issue, since the great circle and the actual ray path are very close to each other if the great circle lies in the influence zone.

The concept of the influence zone also gives us an insight into the validity of the great-circle approximation, which has been widely used in most studies of surface wave tomography. Since the influence zone is defined so that the waveforms within the area are coherent, we may say that phases of surface waves along rays passing out of the influence zone are no longer coherent with the phase along the central ray path. In other words, if the great circle lies outside of the estimated influence zone for a model, the waves along an actual ray and the corresponding great circle should be significantly different, which may result in mislocation of heterogeneity in tomographic models.

Since the FRT approach relies on paraxial ray theory, which is based on a high-frequency approximation, a velocity structure should not vary appreciably within the width of the Fresnel area. Recent tomography models in regional scales (e.g. Debayle & Kennett 2000) have shown quite large velocity variations (over ± 10 per cent) in the uppermost mantle, although these models are still derived from the assumption of wave propagation along the great circle. Such models with moderate lateral heterogeneities seem to be at the limit of the ray-based technique and the great-circle approximation is about to be violated. Even though our approach is still based on similar limitations to the conventional ray theory, we may slightly extend the limit of the ray-based method by introducing ray tracing and considering the effects from surrounding regions about a surface wave ray path to take into account the off-great-circle propagation as well as the finite-frequency effects.

The method of FRT is simple and computationally effective and, therefore, allows us to apply it in large-scale inversions. Although the scattered waves coming from outside the influence zone cannot be fully treated with our approach, such scattering effects seem not be so important in the intermediate period range (40–150 s). We are now able to deal with ray paths with finite widths as well as the deviations in propagation from the great circle in a simple, computationally efficient form. The recent development of a technique of the multimode dispersion measurements for regional surface waves (Yoshizawa & Kennett 2002a) allows us to reconstruct multimode phase-speed maps on regional scales. Together with such multimode information and the influence zone for phase-speed structures, we can envisage a new approach for reconstructing a 3-D image of the upper mantle from multimode surface waves (Kennett & Yoshizawa 2002). The concept of the influence zone presented here should be of great help in extending the current methods of surface wave tomography, which have commonly been based on geometrical ray theory and on the approximation of great-circle propagation.

ACKNOWLEDGMENTS

We thank E. Debayle for the provision of velocity models. We are also grateful to F. A. Dahlen and A. Lomax for their useful comments. KY wishes to thank K. Yomogida for discussions concerning the surface wave Fresnel zone.

REFERENCES

Aki, K. & Richards, P.G., 1980. *Quantitative Seismology, Theory and Methods,* Freeman, San Francisco, CA.

Born, M. & Wolf, E., 1999. *Principles of Optics,* 7th edn, Cambridge University Press, Cambridge.

Červený, V., 1985. The application of ray tracing to the numerical modeling of seismic wave fields in complex structures, in *Seismic Shear Waves, Part A: Theory,* pp. 1–124, ed. Dohr, G., Geophysical Press, London.

Červený, V., 1987. Ray tracing algorithms in three-dimensional laterally varying layered structures, in *Seismic Tomography,* pp. 99–133, ed. Nolet, G., Reidel, Dordrecht.

Červený, V. & Soares, J.E.P., 1992. Fresnel volume ray tracing, *Geophysics,* **57,** 902–915.

Červený, V., Klimeš, L. & Pšenčik, I., 1988. Complete seismic-ray tracing in three-dimensional structures, in *Seismological Algorithms,* pp. 89–168, ed. Doornbos, D.J., Academic Press, London.

Dahlen, F.A. & Tromp, J., 1998. *Theoretical Global Seismology,* Princeton University Press, Princeton, NJ.

Dahlen, F.A., Hung, S.-H. & Nolet, G., 2000. Fréchet kernels for finite-frequency travel times—I. Theory, *Geophys. J. Int.,* **141,** 157–174.

Debayle, E. & Kennett, B.L.N., 2000. The Australian continental upper mantle: structure and deformation inferred from surface waves, *J. geophys. Res.,* **105,** 25 423–25 450.

Hung, S.-H., Dahlen, F.A. & Nolet, G., 2000. Fréchet kernels for finite-frequency travel times—II. Examples, *Geophys. J. Int.,* **141,** 175–203.

Jobert, N. & Jobert, G., 1987. Ray tracing for surface waves, in *Seismic Tomography,* pp. 275–300, ed. Nolet, G., Reidel, Dordrecht.

Kennett, B.L.N., 1983. *Seismic Wave Propagation in Stratified Media,* Cambridge University Press, Cambridge.

Kennett, B.L.N., 1984. Guided wave propagation in laterally varying media—I. Theoretical development, *Geophys. J. R. astr. Soc.,* **79,** 235–255.

Kennett, B.L.N. & Nolet, G., 1990. The interaction of the *S*-wavefield with upper mantle heterogeneity, *Geophys. J. Int.,* **101,** 751–762.

Kennett, B.L.N. & Yoshizawa, K., 2002. A reappraisal of regional surface wave tomography, *Geophys. J. Int.,* in press.

Li, X.-D. & Romanowicz, B., 1995. Comparison of global waveform inversions with and without considering cross-branch modal coupling, *Geophys. J. Int.,* **121,** 695–709.

Li, X.-D. & Tanimoto, T., 1993. Waveforms of long-period body waves in a slightly aspherical Earth model, *Geophys. J. Int.,* **112,** 92–102.

Luo, Y. & Shuster, G.T., 1991. Wave-equation traveltime inversion, *Geophysics,* **56,** 645–653.

Marquering, H. & Snieder, R., 1995. Surface-wave mode coupling for efficient forward modelling and inversion of body-wave phases, *Geophys. J. Int.,* **120,** 186–208.
Marquering, H., Nolet, G. & Dahlen, F.A., 1998. Three-dimensional waveform sensitivity kernels, *Geophys. J. Int.,* **132,** 521–534.
Marquering, H., Dahlen, F.A. & Nolet, G., 1999. Three-dimensional sensitivity kernels for finite-frequency travel times: the banana–doughnut paradox, *Geophys. J. Int.,* **137,** 805–815.
Meier, T., Lebedev, S., Nolet, G. & Dahlen, F.A., 1997. Diffraction tomography using multimode surface waves, *J. geophys. Res.,* **102,** 8255–8267.
Nataf, H.C. & Ricard, T., 1996. 3SMAC: an *a priori* tomographic model of the upper mantle based on geophysical modeling, *Phys. Earth planet. Inter.,* **95,** 101–122.
Snieder, R., 1986. 3-D linearized scattering of surface waves and a formalism for surface wave holography, *Geophys. J. R. astr. Soc.,* **84,** 581–605.
Snieder, R., 1987. On the connection between ray theory and scattering theory for surface waves, in *Mathematical Geophysics,* pp. 77–83, eds Vlaar, N.J., Nolet, G., Wortel, M.J.R. & Cloetingh, S.A.P.L., Reidel, Dordrecht.
Tromp, J. & Dahlen, A.F., 1992a. Variational principles for surface wave propagation on a laterally heterogeneous Earth—I. Time-domain JWKB theory, *Geophys. J. Int.,* **109,** 581–598.
Tromp, J. & Dahlen, A.F., 1992b. Variational principles for surface wave propagation on a laterally heterogeneous Earth—II. Frequency-domain JWKB theory, *Geophys. J. Int.,* **109,** 599–619.
Vasco, D.W. & Majer, E.L., 1993. Wavepath traveltime tomography, *Geophys. J. Int.,* **115,** 1055–1069.
Vasco, D.W., Peterson, J.E. & Majer, E.L., 1995. Beyond ray tomography: wavepath and Fresnel volumes, *Geophysics,* **60,** 1790–1804.
Wang, Z. & Dahlen, F.A., 1995. Validity of surface-wave ray theory on a laterally heterogeneous earth, *Geophys. J. Int.,* **123,** 757–773.
Woodhouse, J.H., 1974. Surface waves in a laterally varying layered structure, *Geophys. J. R. astr. Soc.,* **37,** 461–490.
Woodhouse, J.H. & Wong, Y.K., 1986. Amplitude, phase and path anomalies of mantle waves, *Geophys. J. R. astr. Soc.,* **87,** 753–773.
Woodward, M.J., 1992. Wave-equation tomography, *Geophysics,* **57,** 15–26.
Yomogida, K., 1985. Gaussian beams for surface waves in laterally slowly-varying media, *Geophys. J. R. astr. Soc.,* **82,** 511–533.
Yomogida, K., 1988. Surface waves in weakly heterogeneous media, in *Mathematical Geophysics,* pp. 53–75, eds Vlaar, N.J., Nolet, G., Wortel, M.J.R. & Cloetingh, S.A.P.L., Reidel, Dordrecht.
Yomogida, K., 1992. Fresnel zone inversion for lateral heterogeneities in the Earth, *Pure appl. Geophys.,* **138,** 391–406.
Yomogida, K. & Aki, K., 1985. Waveform synthesis of surface waves in a laterally heterogeneous earth by the Gaussian beam method, *J. geophys. Res.,* **90,** 7665–7688.
Yomogida, K. & Aki, K., 1987. Amplitude and phase data inversion for phase velocity anomalies in the Pacific Ocean basin, *Geophys. J. R. astr. Soc.,* **88,** 161–204.
Yoshizawa, K. & Kennett, 2002a. Nonlinear waveform inversion for surface waves with a neighbourhood algorithm—application to multi-mode dispersion measurements, *Geophys. J. Int.,* in press.
Zhao, L., Jordan, T.H. & Chapman, C.H., 2000. Three-dimensional Fréchet differential kernels for seismic delay times, *Geophys. J. Int.,* **141,** 558–576.

APPENDIX A: PARAXIAL RAY APPROXIMATION IN A RAY-CENTRED COORDINATE SYSTEM

In this appendix, we will derive an explicit formulation for a second partial derivative of ψ based on the paraxial ray approximation. We first consider the Taylor expansion of the phase ψ around a point on the ray $(s, 0)$ at fixed s,

$$\psi(s,n) = \psi(s,0) + n\left.\frac{\partial\psi(s,n)}{\partial n}\right|_{n=0} + \frac{1}{2}n^2\left.\frac{\partial^2\psi(s,n)}{\partial n^2}\right|_{n=0}. \quad \text{(A1)}$$

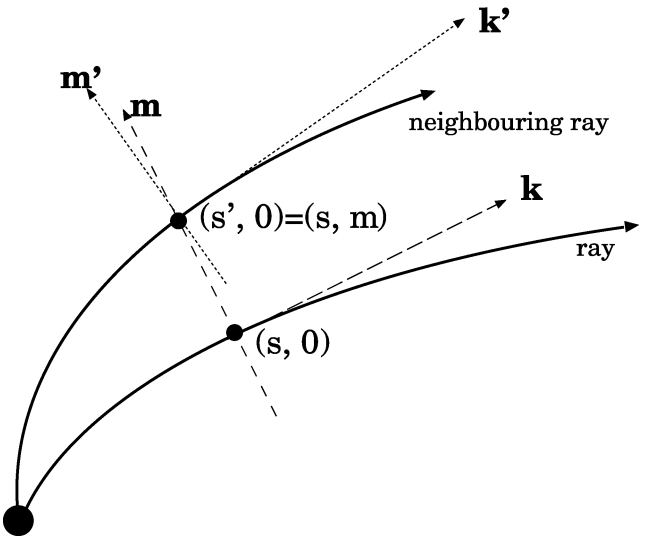

Figure A1. Ray coordinate system. (s, m) is evaluated from a ray passing through that point and another orthogonal coordinates (s', m') is introduced for all rays. So that the direction of m is always perpendicular the ray and tangent to the wave front.

Since the wave front is perpendicular to the ray in ray-centred coordinates,

$$\left.\frac{\partial\psi(s,n)}{\partial n}\right|_{n=0} = 0, \quad \text{(A2)}$$

and so the phase ψ at (s, n) can be expressed as

$$\psi(s,n) = \psi(s,0) + \frac{1}{2}n^2 M(s), \quad \text{(A3)}$$

where $M(s) = \partial_n^2\psi(s,n)|_{n=0}$.

Following Yomogida (1988), $M(s)$ can be determined from the geometrical spreading evaluated at $(s, 0)$. For the time being, let us introduce a 'ray' coordinate system (s, m) (Fig. A1). This coordinate system is different from the 'ray-centred' coordinate system. In ray-centred coordinates, the central ray is fixed and a neighbouring point (s, n) is represented by a perpendicular distance n from a point $(s, 0)$ on the central ray (Fig. 3), whilst in ray coordinates, s is measured along a different ray path passing through the point (s, m) which is under consideration. In other words, we need to consider different coordinates for points on different ray paths as seen in Fig. A1. For the points on the central ray in a ray-centred coordinate system, the 'ray' (s, m) and 'ray-centred' (s, n) coordinates will be the same.

In the ray coordinates for 2-D case, the Laplacian of the phase ψ can be written as

$$\nabla^2\psi = \frac{1}{h_1 h_2}\left[\frac{\partial}{\partial s}\left(\frac{h_2}{h_1}\frac{\partial\psi}{\partial s}\right) + \frac{\partial}{\partial m}\left(\frac{h_1}{h_2}\frac{\partial\psi}{\partial m}\right)\right], \quad \text{(A4)}$$

where h_1 and h_2 are scaling factors for s and m, respectively. In this rey-coordinate scheme, s is always a tangent to the ray path and m is perpendicular to the ray path, resulting in

$$\frac{\partial\psi}{\partial s} = k = \frac{\omega}{c}, \quad \frac{\partial\psi}{\partial m} = 0. \quad \text{(A5)}$$

Substituting (A5) into (A4) with the scaling factors $h_1 = 1, h_2 = J$,

$$\nabla^2\psi = \frac{\omega}{J}\left[\frac{\partial}{\partial s}\left(\frac{J}{c}\right)\right] = \frac{\partial}{\partial s}\left(\frac{\omega}{c}\right) + \frac{\omega}{cJ}\frac{dJ}{ds}, \quad \text{(A6)}$$

where the constant J is assumed to be a function of s. The scaling factor $h_2 = J$ corresponds to the geometrical spreading.

Next let us return to ray-centred coordinates (s, n) and investigate the relation between M and J. By differentiating (A3) with respect to s and n,

$$\frac{\partial \psi}{\partial s} = k + \frac{1}{2} n^2 \frac{dM}{ds}, \tag{A7}$$

$$\frac{\partial \psi}{\partial n} = Mn. \tag{A8}$$

The Laplacian of the phase ψ in this case can be obtained from (A7) and (A8),

$$\nabla^2 \psi|_{n=0} = \left(\frac{\partial^2 \psi}{\partial s^2} + \frac{\partial^2 \psi}{\partial n^2} \right)_{n=0} = \frac{\partial}{\partial s} \left(\frac{\omega}{c} \right) + M(s). \tag{A9}$$

We then find the relation between M and J by comparing (A6) and (A9),

$$M(s) = \frac{\omega}{c(s) J(s)} \frac{dJ(s)}{ds}. \tag{A10}$$

Since we already know the geometrical spreading J as in eq. (13), the evaluation of $M(s)$ is straightforward.

In (A10), we need to differentiate J with respect to s. This can be done analytically using eq. (13) and the derivative can be expressed in terms of the solutions of the DRT eqs (6)–(8),

$$\frac{dJ}{ds} = \frac{1}{J} \left[-\sin\zeta \frac{\partial \theta}{\partial \zeta_0} \frac{\partial \zeta}{\partial \zeta_0} + \sin\theta \frac{\partial \phi}{\partial \zeta_0} \left(\cos\theta \cos\zeta \frac{\partial \phi}{\partial \zeta_0} - \cot\theta \sin\zeta \frac{\partial \theta}{\partial \zeta_0} + \cos\zeta \frac{\partial \zeta}{\partial \zeta_0} \right) \right]. \tag{A11}$$

APPENDIX B: CORRECTION OF THE PARAXIAL FRESNEL AREA AT SOURCE AND RECEIVER

The radius of the paraxial Fresnel area in eq. (23) shrinks to 0 at the source and receiver locations because the geometrical spreading J disappears there. However, as seen in Fig. 6, the exact Fresnel area should have a finite radius even at such singular points. Correction of the paraxial Fresnel area can be made by considering the simple geometry around the source and the receiver (Fig. B1).

We pay attention only to the source region as shown in Fig. B1. To extend the paraxial Fresnel area around the source location, it is sufficient to consider two points F_a and F_b. Let us consider a path AF_aB; in the far field, we can expect $\Delta_A^{F_a} \ll \Delta_A^B$, so that $\Delta_A^B \approx \Delta_B^{F_a}$. Using eq. (24), the radius of the paraxial Fresnel area $\Delta_A^{F_a}$ at the source can be given as

$$\Delta_A^{F_a} \approx \frac{\lambda}{2}. \tag{B1}$$

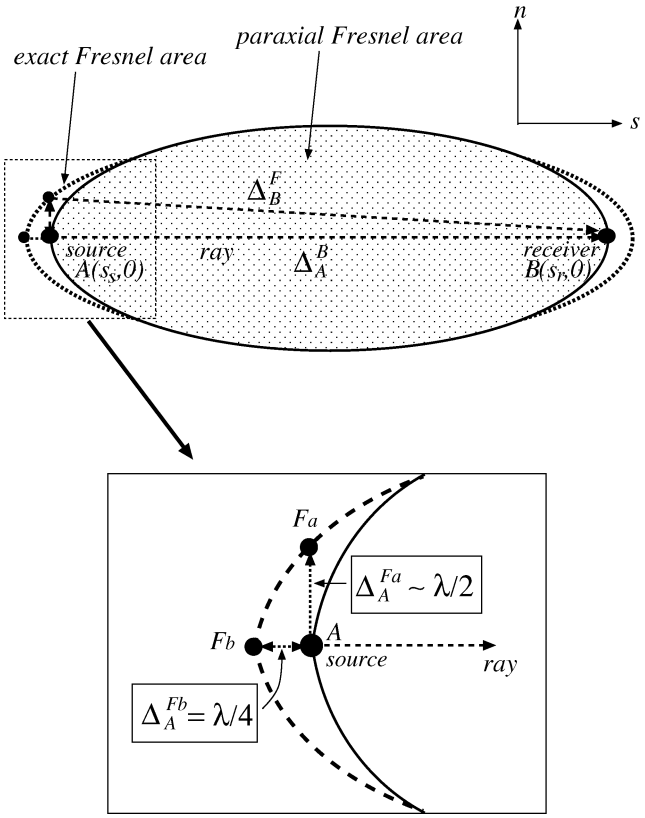

Figure B1. Illustration of the correction of the paraxial Fresnel area at the source and the receiver.

For a path AF_b B along the ray, we can extend the paraxial Fresnel area slightly over the source position. In this case, $\Delta_B^F = \Delta_A^F + \Delta_A^B$. Inserting this relation into eq. (24),

$$\Delta_A^{F_b} = \frac{\lambda}{4}. \tag{B2}$$

The location of the point F_b relative to the source can be obtained from an extrapolation along the ray.

The extended paraxial Fresnel area can be obtained from interpolation of such points surrounding the source on the boundary of the first Fresnel zone. The corrections for the receiver and caustics can be similarly made by following the same procedure as above. The correction of the influence zone at these points is obtained in a similar fashion; we can evaluate the radius of the zone to be one-third of that of the first Fresnel zone, i.e. $\Delta_A^{F_a} \sim \lambda/6$ and $\Delta_A^{F_b} \sim \lambda/12$.